

## Article

# Paleotectonic Stress and Present Geostress Fields and Their Implications for Coalbed Methane Exploitation: A Case Study from Dahebian Block, Liupanshui Coalfield, Guizhou, China

Jilin Wang <sup>1,2,\*</sup> , Youkun Wang <sup>3</sup>, Xiaozhi Zhou <sup>1,2</sup>, Wenxin Xiang <sup>1,2</sup> and Changran Chen <sup>1,2</sup>

<sup>1</sup> Key Laboratory of CBM Resources and Reservoir Formation Process, Ministry of Education (China University of Mining and Technology), Xuzhou 221116, China

<sup>2</sup> School of Resources and Geoscience, China University of Mining and Technology, Xuzhou 221116, China

<sup>3</sup> Guizhou Coalbed Methane Energy Development Co., Ltd., Guiyang 550081, China

\* Correspondence: wang4437@cumt.edu.cn; Tel.: +86-516-83591000

**Abstract:** The macroscopic structural fractures (joints) and geostress distribution characteristics of coal reservoirs are important factors affecting the exploitation of coalbed methane (CBM). In this study, the joints in the sedimentary strata of the Dahebian block in Liupanshui area, Guizhou Province were investigated. Directional coal samples were collected for observation and statistical analysis of coal microfractures, the paleotectonic stress fields of the study area were reconstructed, and the tectonic evolution was elucidated. The geostress distribution characteristics of the target coal seam (coal seam No. 11, P<sub>3</sub>l) in the study area were analyzed using the finite element numerical simulation method. The results indicate that the structural evolution of the Dahebian syncline in the study area can be divided into two stages. The Late Jurassic–Early Cretaceous stage (Early Yanshanian) is the first stage. Affected by the sinistral strike slip of the Weining–Ziyun–Luodian (WZL) fault zone, the derived stress field in the study area exhibits maximum principal stress ( $\sigma_1$ ) in the NEE–SWW direction. The Late Cretaceous stage (Late Yanshanian) is the second stage. Affected by the dextral strike slip of the WZL fault zone, the derived stress field exhibits  $\sigma_1$  in the NNW–SSE direction. The folds and faults formed in the first stage were modified by the structural deformation in the second stage. The dominant strikes of joints in the sedimentary strata are found to be in the NW–NNW (300°–360°) and NE (30°–60°) directions, with dip angles mostly ranging from 60° to 90°. The dominant strikes of coal microfractures are in the NW (285°–304°) and NE (43°–53°) directions. The distribution of geostress in the study area is characterized by high levels of geostress in the syncline center, decreasing towards the surrounding periphery. The overall trend of the geostress contour line is similar to the shape of the syncline and is influenced by folds and faults. The  $\sigma_1$  of coal seam No. 11 is vertical stress. The prediction results show that the joint density of coal seam No. 11 in the block is 36–50 joints/m, and the shape of the joint density contour line is also affected by the axial direction of the Dahebian syncline and the surrounding faults. The variation in coal seam joint density and the control effect of geostress on joints opening or closing affects the permeability of coal reservoirs. The study results provide significant guidance for the exploitation of CBM.

**Keywords:** joint; natural fractures; tectonic stress field; geostress; coalbed methane



**Citation:** Wang, J.; Wang, Y.; Zhou, X.; Xiang, W.; Chen, C. Paleotectonic Stress and Present Geostress Fields and Their Implications for Coalbed Methane Exploitation: A Case Study from Dahebian Block, Liupanshui Coalfield, Guizhou, China. *Energies* **2024**, *17*, 101. <https://doi.org/10.3390/en17010101>

Academic Editor: Dameng Liu

Received: 25 October 2023

Revised: 4 December 2023

Accepted: 11 December 2023

Published: 23 December 2023



**Copyright:** © 2023 by the authors. Licensee MDPI, Basel, Switzerland. This article is an open access article distributed under the terms and conditions of the Creative Commons Attribution (CC BY) license (<https://creativecommons.org/licenses/by/4.0/>).

## 1. Introduction

Coal is typically considered as naturally fractured reservoir rocks with their fractures providing the main pathways for gas and fluid flow [1]. The natural fractures in coal seams include endogenous fractures (cleats) and exogenous fractures. The exogenous fractures that are represented by structural fractures can effectively improve the permeability of coalbed methane (CBM) reservoirs, which is conducive to the productivity of CBM wells [2]. Many pores and fractures with different widths and lengths are found in coal, most of which are isolated. The microfractures serve as a bridge for gas migration between pores, cleats,

and macrofractures. The contribution to coal reservoir permeability originates primarily from first- and second-class microfractures [3]. The permeability of CBM reservoirs is highly correlated with its fractures. Research on the fracture permeability model of a CBM reservoir with a high-dip angle in the southern Junggar Basin, northwest China, has been verified by well tests [4]. In the case of constant total fracture length, number, and spacing, when fracture half-lengths are in a long and short interlaced distribution, the CBM production is the highest, corresponding to the best fracture distribution pattern [5]. Studies have shown that the variable shape distribution (VSD) method is an advanced fractal method for characterizing the distribution characteristics of natural fractures [6].

The joint orientation is controlled by the stress field in which the joints propagate. Thus, most joint orientation distributions in bedded rocks have a non-random variation and are greater in the strike than in the dip orientation [7]. Joints and shear fractures are sensitive signs of changes in the microstress field; thus, they are widely distributed and have important characteristics of consistent orientation in the region, which can be used to restore the state and evolution process of the regional stress field [8]. By observing data of conjugate shear joints in the field and even in the underground of the study area and using the stereographic projection method to analyze the data of the conjugate shear joints, the paleotectonic stress field experienced in the study area can be inferred, as in the study of the tectonic stress fields in the Indosinian, Yanshanian, and Himalayan periods in the mining area of Pingdingshan, China [9], and the reconstruction of the end-late Paleozoic tectonic stress field by natural fractures at the southern edge of Junggar Basin, China [10]. Through microtectonic studies of oriented samples, the characteristics of the regional tectonic stress can also be obtained [11]. With the application of multiple periods of stress, the tectonic superposition areas usually have complex spatial relationships. The fracture development period in the area can be identified by separating and extracting the superposed fracture sets [12], or the tectonic stress in the study area can be reconstructed using conjugated joints and slickensides [13].

The regional tectonic stress can be analyzed using rose diagrams of joint and stereographic projection. The intersection line of conjugate shear joints is parallel to the middle principal stress axis ( $\sigma_2$ ). Their included angle bisectors are maximum ( $\sigma_1$ ) and minimum ( $\sigma_3$ ) principal stress axes. After determining the orientations of  $\sigma_1$  and  $\sigma_3$ , the trajectory lines of the principal stress network can be drawn according to the data of many observed points [14]. Numerical simulation is an important means of studying the stress field. Many scholars have used the finite element simulation method to study the paleotectonic stress field [15–17]. Numerical simulation is also widely used to study the modern tectonic stress field. Some scholars have obtained the geostress field of the coal seam floor by building geological profile models and using the finite element simulation method [18], or have studied the stress field near faults by combining different inversion methods [19].

A previous study showed that the stress state of the coal bed controls joint opening and permeability and that the permeability of the coal bed exhibits a good exponential relationship with the density of the predominant joint set [20]. There is a close relationship between the fracture volume and the stress–strain of coal reservoirs. Several quantitative geomechanical models have been established on the basis of the relationship between fracture and stress parameters. Combined with finite element simulation, the fractures of a coal reservoir can be predicted [21–23]. In the hydraulic fracturing of CBM development, the stress state of the coal reservoir also affects the shape, type, and expansion direction of fractures [24,25]. Clarifying the advantageous orientation of fractures and the principal stress orientation in coal reservoirs can be beneficial in the design of CBM wells [11].

Previous studies have reported significant achievements in relation to the characteristics of natural fractures in coal-bearing strata (or coal reservoirs) and the correlation between fractures and tectonic stress fields. Joint is namely the macroscopic structural fracture. Due to difficulties with direct measurement of coal seam joints in large areas, more studies are needed on the development characteristics of macroscopic fractures in coal seams. Based on the extensive investigation of sedimentary strata joints in the Dahebian

CBM block in Liupanshui, Guizhou, in this paper, we attempt to analyze the paleotectonic stress causes of joints, discuss the influence of modern geostress on the opening or closing of joints, and indirectly predict joints in coal seams through rock joints. We hope that this study will assist in the process of improving CBM exploitation.

## 2. Geologic Setting, History, and Development Characteristics of Joints

### 2.1. Geological Conditions in the Study Area

The study area, Dahebian CBM block, is located in the north of the urban area of Liupanshui City, Guizhou Province, 15 km away from Liupanshui City in a straight line, with an area of 46.11 km<sup>2</sup>. The block covers the axis and two wings of the Dahebian syncline. The study area belongs to the plateau middle mountain and karst–tectonic landform, with a surface elevation of 1640–2122 m and a relative elevation difference of approximately 482 m.

The exposed strata in the study area are from the Lower Carboniferous Permian to the Middle Triassic. From the old to the new, the strata exposed in the core and wings of the Dahebian syncline are Emeishan basalt formation ( $P_3\beta$ ), Longtan formation ( $P_3l$ ), Feixianguan formation ( $T_1f$ ), Yongningzhen formation ( $T_1yn$ ), and Guanling formation ( $T_2g$ ) (Table 1). The main structural form of the study area is the Dahebian syncline, a wide and gentle syncline formed in the Early to Middle Yanshanian. The fold was reformed in the Late Yanshanian, so the fold axis now extends NW–SE in the north–middle and NE–SW in the south. The dip angle of the strata is approximately 14°–21°, and the dip angle in the east of the syncline axis is relatively larger. Most of the faults developed in the study area are reverse faults, with very few normal faults (also with strike-slip properties) and a few faults with unidentified properties (which should be the same as other faults). Based on the properties and strikes of the faults, it is speculated that they are formed and reformed simultaneously with the folds. The adjacent Shenxianpo syncline and Tudiya syncline are developed outside the northeast–east edge of the block, with the same formation stage as the Dahebian syncline (Figure 1).

**Table 1.** Regional stratigraphic lithologies.

Stratigraphic Unit				Thickness (m) Min– Max/Average	Main Lithology	Mechanical Property	
Erathem	System	Series	Group (Code)				
Cenozoic	Quaternary			0–8	Loose deposits.		
			Middle Triassic	Guanling ( $T_2g$ )	>500	Mudstone intercalated with marlstone in the lower part; limestone and dolomitic limestone in the upper part.	Hard
		Mesozoic	Triassic	Lower Triassic	Yongningzhen ( $T_1yn$ )	144.00– 330.00/237.00	Argillaceous dolomite and mudstone in the upper part; dolomitic limestone, argillaceous limestone and limestone in the middle and lower parts; argillaceous limestone in the bottom.
				91.49– 97.40/93.72	Siltstone, silty mudstone, and mudstone intercalated with limestone and argillaceous limestone.	Medium soft	

Table 1. Cont.

Stratigraphic Unit				Thickness (m) Min– Max/Average	Main Lithology	Mechanical Property	
Erathem	System	Series	Group (Code)				
Paleozoic	Permian	Upper Permian	Feixianguan (T <sub>1f</sub> )	92.77– 124.55/111.61	Limestone occasionally intercalated with thin layers of argillaceous limestone.	Hard	
				106.76– 134.06/120.45	Fine sandstone, siltstone, and mudstone.	Medium hard	
				244.23– 289.63/262.08	Fine sandstone, siltstone, silty mudstone, and mudstone intercalated with fine sandstone and limestone.		
				99.87– 118.14/110.29	Medium-thick layered fine sandstone, siltstone, and thin limestone.	Hard	
		Upper Permian	Longtan (P <sub>3l</sub> )	71.44– 102.61/88.62	Fine sandstone, siltstone, argillaceous siltstone, and coal seam. Argillaceous rocks are dominant.	Soft	
				4.73–9.63/6.42	Coal seam No. 11 (target seam).	Extremely soft	
				23.23– 50.89/34.70	Mudstone, argillaceous siltstone, siltstone, and coal seam. Argillaceous rocks are dominant.	Soft	
				74.61– 151.53/103.87	Fine sandstone, siltstone, argillaceous siltstone, and coal seam. Argillaceous rocks are dominant.		
				Middle Permian	Emeishan basalt (P <sub>3β</sub> )	100–200	Tuff and basalt.
		Maokou (P <sub>2m</sub> )	350–420			Limestone.	Hard
			Qixia (P <sub>2q</sub> )			120–150	
		Lower Permian	Liangshan (P <sub>1l</sub> )	10–50	Quartz sandstone, clay rock, and thin coal seam.	Medium soft	
		Carboniferous	Upper Carbonif- erous	Mapping (C <sub>2mp</sub> )	70–240	Limestone locally intercalated with chert nodules or dolomite.	Hard
Huanglong (C <sub>2h</sub> )	80–200			Limestone and dolomite.			
Lower Carbonif- erous	Baizuo (C <sub>1b</sub> )		>200	Dolomitic limestone intercalated with chert nodules or bands.			

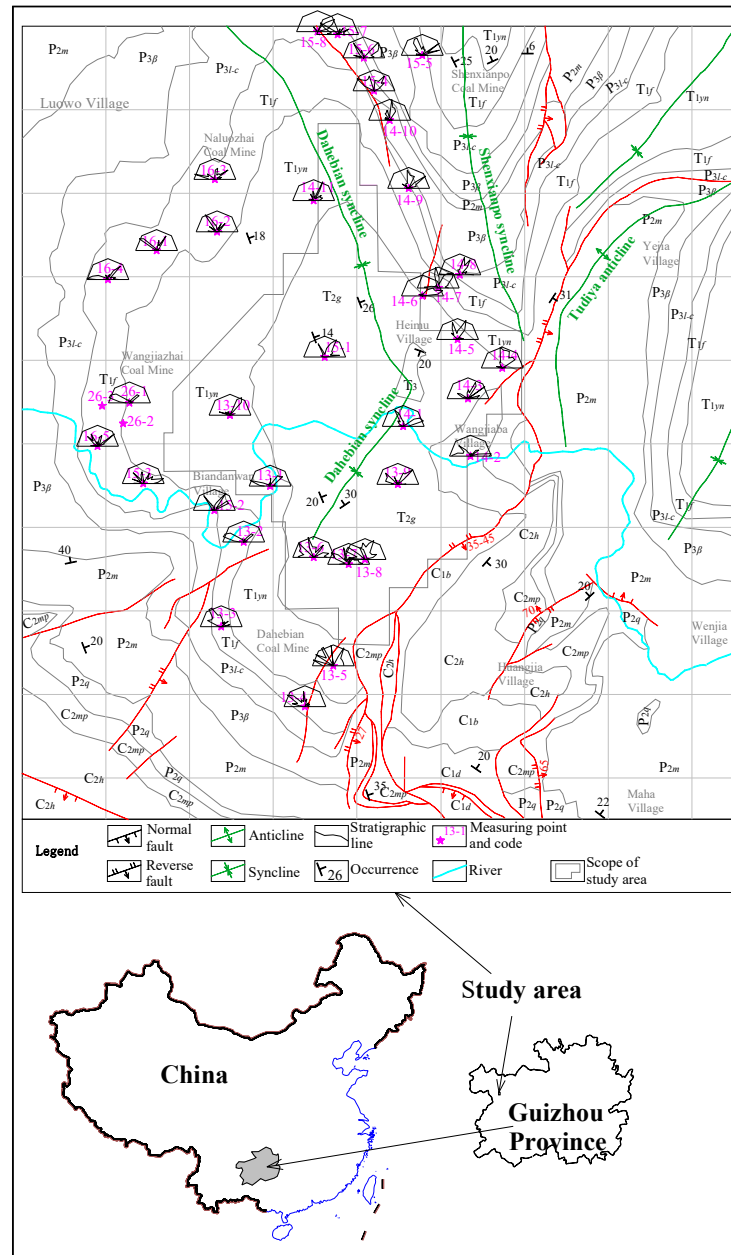


Figure 1. Structural outline of the study area.

The CBM geology in Guizhou is characterized by high gas content, pressure, and resource abundance, indicating superior CBM resource potential [26]. There are a total of 40 coal seams in the Dahebian block in Liupanshui coalfield, with a minable thickness of about 20 m. The total potential coal resources are 103.881 million tons [27].

### 2.2. Geological Development History of Coal-Bearing Basin

Early structural studies suggest that the fold and fault zones in central and western Guizhou, including the Liupanshui coalfield, are controlled by cross faults in the basement zone. The current tectonic pattern was formed during the Yanshanian, showing arc, diamond, triangle, and other structural combinations [28,29]. The Liupanshui coalfield, where the study area is located, is more closely related to the WZL fault zone distributed in the west of Guizhou. This fault zone is a large intracontinental fault on the southern margin of the Yangtze plate. It starts from Weining County in Yunnan Province in the north, passes through Ziyun County in Guizhou Province, and ends in Luodian County in Guizhou

Province in the south. The fault zone was under extension during the Early Devonian to Middle Triassic, which controlled the depositional sequence of the region. The fault zone was deformed during the Indosinian at the end of Triassic. The major deformation occurred during the Early Yanshanian in the Late Jurassic to Early Cretaceous, related to the westward push of the South China block, causing an oblique, sinistral strike-slip deformation [30].

The formation of the Liupanshui coal basin was formed under the control of the Ziyun–Yadou fault (the northwest section of the WZL fault zone) and the Liupanshui fault [31] (Figure 2). Previous studies have shown that the burial depth of coal seams in the Dahebian block exceeds 3000 m in the Early and Middle Triassic. The Yanshanian and Himalayan orogenies since the Late Jurassic have destroyed the prototype of the basin, leading to an inversion of 500–600 m, as well as uplift and erosion [27].

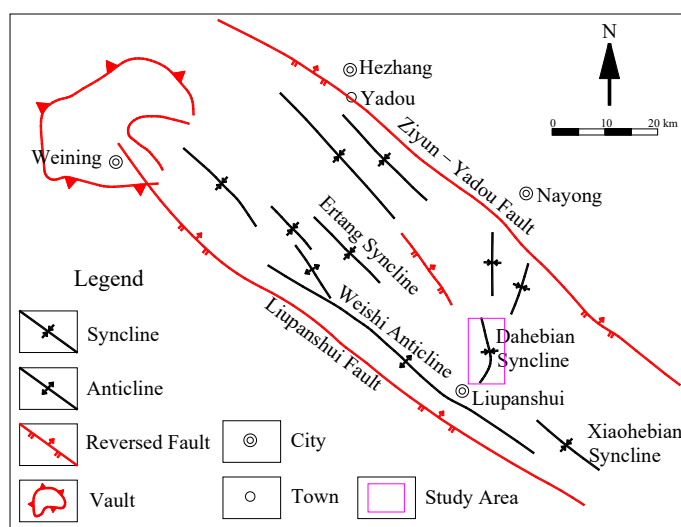


**Figure 2.** Structural outline of Liupanshui area (according to [31], revised).

### 2.3. Development of Joints (Structural Fractures)

A geological field survey of the Dahebian block was carried out, including observation of structural characteristics, outcrop lithology, and joint measurement. Joints are structural fractures with obvious directionality and can be divided into extension joints and shear joints based on their mechanical properties. The measured joints were mainly shear joints, with a few extension joints, because the extension joints were generally uneven on the surface or were filled and inconvenient for measurement. The field geological survey points were scattered throughout the core and wings of the Dahebian syncline, including the sedimentary strata of the Upper Permian to Lower–Middle Triassic, especially the coal-bearing stratum, i.e., the Longtan formation ( $P_3l$ ). The lithology of the strata mainly consists of sandstone, shale, limestone, and coal. A total of 34 outcrops were observed; 1593 joints were measured in the field in the whole area, and 2 points were observed in the underground of the Wangjiazhai coal mine. The dominant orientation of the joint strikes of each observation point was obtained, including the dominant orientation of coal microfractures (Figure 1). The joint linear density (frequency) of each observation point was measured (Table 2).

Table 2. Investigations of joints.

Site	Coordinate		Number of Joints	Linear Density (Counts/m)	Stratum Occurrence (°)	Chrono-Stratigraphy	Lithology
	X	Y					
13-1	18,484,932.14	2,952,009.24	43	3.0	54/36	T <sub>1yn</sub>	Limestone
13-2	18,484,295.28	2,950,646.15	48	3.5	97/23	T <sub>1f</sub>	Sandstone
13-3	18,483,755.76	2,948,619.75	52	8.5	47/29	T <sub>1f</sub>	Mudstone
13-4	18,485,757.53	2,946,694.59	50	6.0	14/7	T <sub>1f</sub>	Sandstone
13-5	18,486,433.12	2,947,675.73	20		45/25	T <sub>1yn</sub>	Limestone
13-6	18,485,968.03	2,950,257.82	40	6.3	90/9	T <sub>2g</sub>	Limestone
13-7	18,486,798.07	2,950,115.88	46	2.5	70/4	T <sub>2g</sub>	Limestone
13-8	18,487,201.78	2,950,219.11	51	4.5	137/3	T <sub>2g</sub>	Limestone
13-9	18,487,977.46	2,952,026.81	31	3.7	333/9	T <sub>2g</sub>	Marlstone
13-10	18,483,968.70	2,953,672.02	49	2.8	115/12	T <sub>1yn</sub>	Limestone
14-1	18,488,103.20	2,953,416.45	50	3.7	150/75	T <sub>2g</sub>	Limestone
14-2	18,489,717.65	2,952,695.31	48	3.8	289/31	T <sub>1yn</sub>	Limestone
14-3	18,489,652.47	2,954,077.50	42	4.7	32/33	T <sub>2g</sub>	Limestone
14-4	18,490,481.23	2,954,810.73	50	3.5	213/53	T <sub>2g</sub>	Limestone
14-5	18,489,410.16	2,955,487.10	41	3.7	204/44	T <sub>2g</sub>	Limestone
14-6	18,488,566.52	2,956,547.91	50	5.3	230/83	T <sub>2g</sub>	Limestone
14-7	18,488,943.42	2,956,740.51	52	8.0	212/54	T <sub>1yn</sub>	Sandstone
14-8	18,489,456.18	2,957,046.93	47	9.3	275/50	P <sub>3l</sub>	Mudstone
14-9	18,488,232.36	2,959,116.58	50	9.5	218/62	T <sub>1f</sub>	Pelitic siltstone
14-10	18,487,790.25	2,960,759.83	40	12.5	225/32.5	P <sub>3β</sub>	Emeishan basalt
14-11	18,485,964.79	2,958,829.55	46	10.0	124/18	T <sub>1yn</sub>	Limestone
15-1	18,486,232.98	2,955,077.59	46	6.3	137/18	T <sub>2g</sub>	Limestone
15-2	18,483,589.82	2,951,397.26	46	5.0	10/46	T <sub>1f</sub>	Pelitic siltstone
15-3	18,481,895.64	2,952,032.88	50	6.7	45/15	T <sub>1f</sub>	Pelitic siltstone
15-4	18,487,403.51	2,961,456.93	64	9.3	205/52	P <sub>2m</sub>	Limestone
15-5	18,488,551.65	2,962,300.89	51	9.5	54/21	P <sub>3l</sub>	Mudstone
15-6	18,487,167.12	2,962,258.02	53	5.3	190/27	P <sub>2m</sub>	Limestone
15-7	18,486,539.70	2,962,785.92	50	15.0		P <sub>3β</sub>	Emeishan basalt
15-8	18,486,064.23	2,962,871.92	38	15.0	235/67	P <sub>3l</sub>	Sandstone
16-1	18,482,200.95	2,957,630.13	52	11.5	138/22	T <sub>1f</sub>	Sandstone
16-2	18,483,658.31	2,958,074.71	50	6.0	119/12	T <sub>1f</sub>	Sandstone
16-3	18,483,600.18	2,959,348.48	51	6.3	164/22	T <sub>1f</sub>	Sandstone
16-4	18,481,053.72	2,956,951.07	46	8.7	110/11	T <sub>1f</sub>	Sandstone
16-5	18,480,800.07	2,952,949.14	50	4.7	45/30	T <sub>1f</sub>	Sandstone

According to the dominant orientations shown in the joint rose map of each measuring point, statistics revealed that the dominant strikes of joints in the sedimentary rock strata in the study area are approximately NW–NNW (300°–360°) and NE (30°–60°) (Figure 3a). The dip angle of joints in the study area is generally large, and joints with dip angles greater than 60° account for 70.9% (Figure 3b). The dominant strikes of coal microfractures are NW (285°–304°) and NE (43°–53°) (Figure 4). Given that the strike direction of coal microfractures is measured by taking photos on a light sheet under a microscope, the dip angle data cannot be obtained.

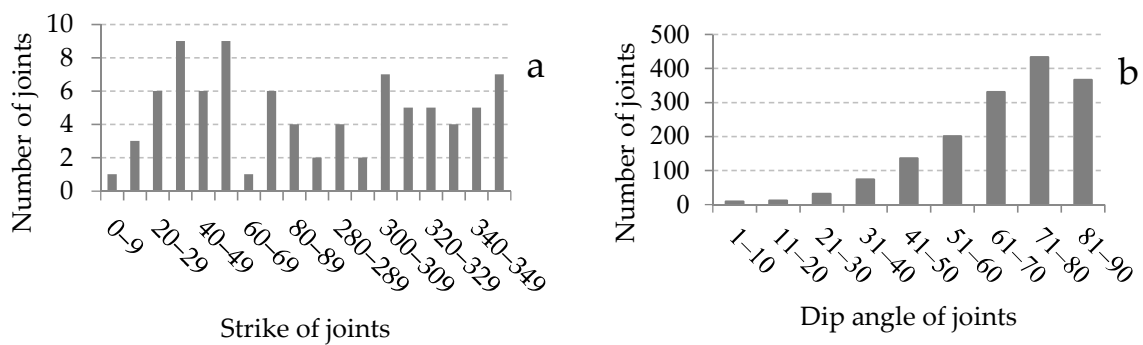


**Figure 3.** Dominant strike (a) and dip angle (b) of joints.

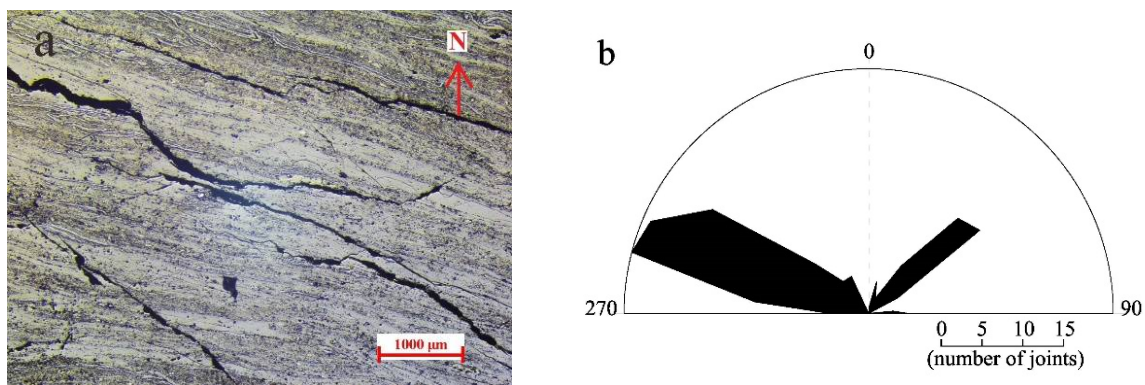


**Figure 4.** Photomicrograph (a) and strike rose diagram (b) of coal microfractures.

### 3. Paleotectonic Stress Field Reconstructions

#### 3.1. Methodology

Joints are always extensively developed in rock strata that have experienced structural deformation. Using a system of conjugate shear joints to restore the paleotectonic stress field is a classical method in structural geology. The bisector of the acute angle of the surface of the conjugate shear joints indicates the maximum principal stress ( $\sigma_1$ ) orientation. The obtuse-angle bisector indicates the minimum principal stress ( $\sigma_3$ ) orientation. According to this principle, staging and matching of conjugate joints can determine the  $\sigma_1$  and  $\sigma_3$  orientations. The application of this method to the analysis of the structural deformation of sedimentary rock strata is feasible. The initial conjugate shear joints are formed in the horizontal state of the rock stratum, and continuous or late tectonic action causes the rock stratum to tilt or even form folds. Therefore, the occurrence of early plane conjugate joints changes. The rock stratum should be restored to the horizontal state to obtain the accurate plane conjugate joint occurrence.

Generally, enough joint occurrences are measured at the outcrop. A joint density map is drawn, and several extremum points of density are obtained. After the rock stratum occurrence is restored to the horizontal state, joint staging and matching are carried out. These operations can be completed through stereographic projection.

#### 3.2. Paleotectonic Stress Fields

From the wider area around the study area, the lithostratigraphy can be seen from the Upper Triassic to the Lower–Middle Jurassic in the center of some synclinal basins, where purplish–red continental conglomerate, sandstone, and shale are deposited. According on the characteristics of the tectonic layer in the study area and previous research results, the study area has experienced two important tectonic stages since the end of the coal-forming period: the terrestrial facies depression stage of  $T_3$ – $J_2$  and the fault-folded uplift stage after  $J_3$  [32]. The main tectonic framework across Guizhou was established during the

Yanshanian. In the Late Jurassic and Early Cretaceous, the crust in the Guizhou region was significantly shortened under nearly east–west compression. The Ziyun–Luodian fault, which has a controlling influence on the study area, underwent different tectonic deformations in the Mesozoic and Cenozoic, including dextral thrusting, sinistral compression, and sinistral strike–slip movement [33].

According to the statistical results relating to the joints in the study area, the dominant joint orientations and combinations are obtained using the joint density stereogram, and the conjugate shear joint system is staged and matched to obtain the principal stress orientation of each measuring point, restoring the paleotectonic stress field. The results show that the tectonic framework in the study area experienced two main stages of the tectonic stress field (Table 3).

**Table 3.** Analysis of principal stress at each measuring point.

Site	Axes	Principal Stress (First Stage)		Principal Stress (Second Stage)		Site	Axes	Principal Stress (First Stage)		Principal Stress (Second Stage)	
		Azimuth (°)	Plunge (°)	Azimuth (°)	Plunge (°)			Azimuth (°)	Plunge (°)	Azimuth (°)	Plunge (°)
13-1	$\sigma_1$	262.9	40.6	/	/	14-8	$\sigma_1$	/	/	125.9	42.3
	$\sigma_2$	62.7	48.0	/	/		$\sigma_2$	/	/	296.1	47.8
	$\sigma_3$	164.2	10.4	/	/		$\sigma_3$	/	/	33.4	6.9
13-2	$\sigma_1$	91.8	17.3	356.4	34.1	14-9	$\sigma_1$	220.2	36.6	/	/
	$\sigma_2$	288.0	71.8	166.2	55.6		$\sigma_2$	57.5	52.5	/	/
	$\sigma_3$	183.4	4.6	263.5	5.1		$\sigma_3$	316.4	8.6	/	/
13-3	$\sigma_1$	253.2	43.2	132.8	/	14-10	$\sigma_1$	54.6	4.6	/	/
	$\sigma_2$	82.0	47.0	/	/		$\sigma_2$	178.7	81.8	/	/
	$\sigma_3$	347.7	4.2	/	/		$\sigma_3$	324.1	6.6	/	/
13-4	$\sigma_1$	81.4	1.3	148.1	15.1	14-11	$\sigma_1$	238.5	17.9	/	/
	$\sigma_2$	327.5	86.5	302.5	73.2		$\sigma_2$	91.1	69.0	/	/
	$\sigma_3$	171.5	2.7	55.9	6.9		$\sigma_3$	331.8	10.2	/	/
13-5	$\sigma_1$	/	/	164.2	15.8	15-1	$\sigma_1$	50.6	29.9	/	/
	$\sigma_2$	/	/	328.3	72.9		$\sigma_2$	228.9	59.4	/	/
	$\sigma_3$	/	/	72.8	4.2		$\sigma_3$	320.5	1.1	/	/
13-6	$\sigma_1$	/	/	319.3	15.2	15-2	$\sigma_1$	/	/	172.6	39.5
	$\sigma_2$	/	/	160.1	73.4		$\sigma_2$	/	/	356.7	50.9
	$\sigma_3$	/	/	50.7	5.5		$\sigma_3$	/	/	264.6	1.7
13-7	$\sigma_1$	253.9	15.2	/	/	15-3	$\sigma_1$	74.4	3.3	340.9	23.2
	$\sigma_2$	58.4	73.9	/	/		$\sigma_2$	186.7	80.6	176.5	65.5
	$\sigma_3$	163.1	4.2	/	/		$\sigma_3$	343.8	8.2	73.8	5.6
13-8	$\sigma_1$	/	/	146.9	12.6	15-4	$\sigma_1$	70.2	8.6	/	/
	$\sigma_2$	/	/	333.4	76.8		$\sigma_2$	189.3	72.5	/	/
	$\sigma_3$	/	/	237.4	1.4		$\sigma_3$	337.9	14.8	/	/
13-9	$\sigma_1$	265.8	3.9	157.8	1.7	15-5	$\sigma_1$	53.4	54.4	128.8	10.6
	$\sigma_2$	37.5	83.8	279.0	86.8		$\sigma_2$	237.8	35.5	328.3	78.6
	$\sigma_3$	175.6	4.4	67.7	2.7		$\sigma_3$	146.5	1.9	219.9	3.6
13-10	$\sigma_1$	253.7	4.3	337.1	8.0	15-6	$\sigma_1$	/	/	130.6	5.7
	$\sigma_2$	126.8	77.6	133.0	81.2		$\sigma_2$	/	/	285.4	83.3
	$\sigma_3$	343.9	5.7	246.6	3.8		$\sigma_3$	/	/	40.5	2.8
14-1	$\sigma_1$	/	/	326.1	19.2	15-8	$\sigma_1$	237.0	21.9	/	/
	$\sigma_2$	/	/	123.7	68.4		$\sigma_2$	50.7	67.6	/	/
	$\sigma_3$	/	/	233.5	7.4		$\sigma_3$	146.3	2.2	/	/

Table 3. Cont.

Site	Axes	Principal Stress (First Stage)		Principal Stress (Second Stage)		Site	Axes	Principal Stress (First Stage)		Principal Stress (Second Stage)	
		Azimuth (°)	Plunge (°)	Azimuth (°)	Plunge (°)			Azimuth (°)	Plunge (°)	Azimuth (°)	Plunge (°)
14-2	$\sigma_1$	52.8	12.4	152.6	41.1	16-1	$\sigma_1$	252.5	13.2	/	/
	$\sigma_2$	257.8	76.1	333.6	49.6		$\sigma_2$	106.6	73.8	/	/
	$\sigma_3$	144.1	5.6	242.8	0.8		$\sigma_3$	344.4	8.6	/	/
14-3	$\sigma_1$	/	/	152.6	45.9	16-2	$\sigma_1$	48.7	11.7	352.1	11.4
	$\sigma_2$	/	/	327.8	44.4		$\sigma_2$	230.7	78.0	174.7	78.1
	$\sigma_3$	/	/	60.2	2.3		$\sigma_3$	138.6	0.5	82.4	0.5
14-4	$\sigma_1$	243.0	3.1	/	/	16-3	$\sigma_1$	68.9	12.0	351.4	11.1
	$\sigma_2$	120.6	83.8	/	/		$\sigma_2$	196.8	70.3	164.2	78.4
	$\sigma_3$	333.4	4.8	/	/		$\sigma_3$	336.0	14.7	261.4	1.3
14-5	$\sigma_1$	55.4	18.2	/	/	16-4	$\sigma_1$	71.0	5.9	/	/
	$\sigma_2$	250.8	70.8	/	/		$\sigma_2$	244.4	83.8	/	/
	$\sigma_3$	146.7	4.8	/	/		$\sigma_3$	341.3	0.7	/	/
14-6	$\sigma_1$	60.1	3.8	/	/	16-5	$\sigma_1$	242.3	6.8	/	/
	$\sigma_2$	273.3	85.4	/	/		$\sigma_2$	16.1	80.1	/	/
	$\sigma_3$	149.9	2.2	/	/		$\sigma_3$	151.5	7.0	/	/

The tectonic stress field of the first stage is illustrated as follows. The  $\sigma_1$  trace is in the NEE–SWW direction, the  $\sigma_3$  trace is in the NNW–SSE direction, and  $\sigma_2$  deflects near the E–W direction in the west–south part and towards the NE–SW direction in the east–north part of the block (Figure 5). The tectonic stress field of the second stage is illustrated as follows. The  $\sigma_1$  trace is in the NNW–SSE direction, the  $\sigma_3$  trace is in the NEE–SWW direction, and the principal stress trace shows a certain degree of fluctuation (Figure 6). The deformation characteristics reflected by the twisted fold axis of the Dahebian syncline and the faults developed in the study area are matched with the two-stage stress field of joint analysis, proving the credibility of the joint analysis from the perspective of regional tectonic deformation.

The analysis revealed that the inclination angle of the  $\sigma_1$  axis was slightly larger at a few measuring points. The shear joint system obtained according to the staging and matching of dominant joints at each measuring point also has certain differences in its orientation, intersected angle, and other parameters. These phenomena should be related to the boundary conditions, rock lithology, and thickness differences in the study area. In general, these local inhomogeneities do not affect the results of stress field analysis. Moreover, the dominant joints of some measuring points are nearly parallel to  $\sigma_1$  and are determined as tensile joints in the stress analysis (such as the first-stage principal stress of 15-5; Figure 5), which is also consistent with the stress field.

### 3.3. Discussion of the Tectonic Evolution of the Study Area

Dong et al. [34] proposed dividing the Yanshanian orogeny into three stages based on a systematic summary of previous research: the strong compression intracontinental orogeny stage (main episode of Yanshanian orogeny,  $165 \pm 5$  Ma–136 Ma), the main extensional collapse and lithospheric thinning stage (135–100 Ma), and the weak compression deformation stage (late episode of Yanshanian orogeny, 100–83 Ma). Its main episode is equivalent to the Early Yanshanian orogeny (Late Jurassic–Early Cretaceous). Due to the subduction of the ancient Pacific plate, the Guizhou region suffered from strong east–west compression, leading to reverse compression and sinistral strike slip of the WZL fault zone [30,33]. Its late episode is equivalent to the Late Yanshanian orogeny (Late Cretaceous).

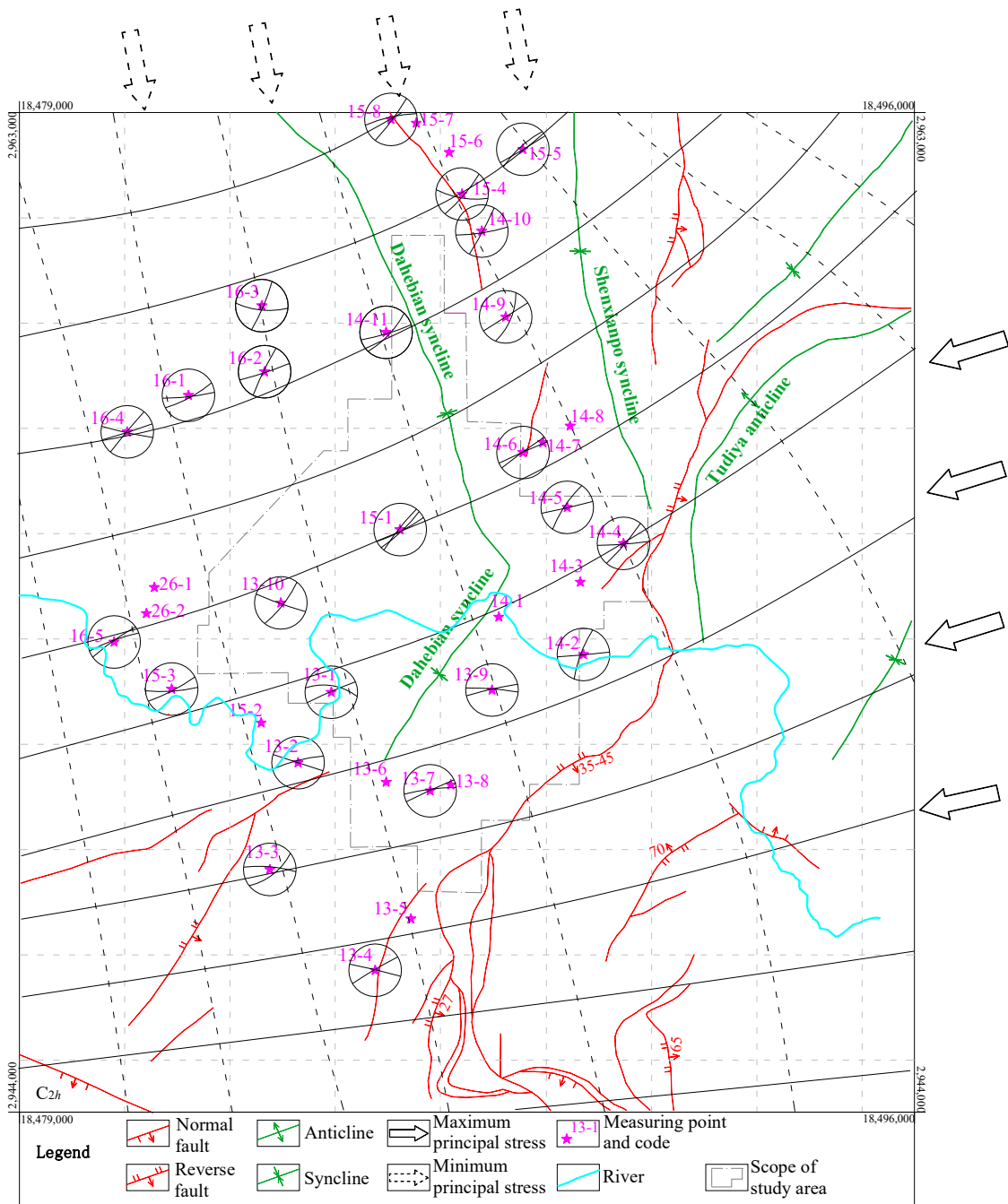


Figure 5. Trace line of the stress field in the first tectonic stage.

To date, only a few studies have covered the Late Yanshanian orogeny of the Chinese mainland. Dong et al. [34] proposed that this era is a weak compression deformation stage. This is consistent with Wan and Zhu's [35] suggestion that the Cretaceous–Early Eocene Chinese mainland presents maximum principal compressive stress in a NNE–SSW direction. Although their time constraints are not completely consistent, they provide a basis for stress field analysis in the Dahebian block. Combined with the regional tectonic evolutionary background, the two stages of tectonic deformation in the study area roughly correspond to the Early Yanshanian (Late Jurassic–Early Cretaceous) and Late Yanshanian (Late Cretaceous).

The WZL fault zone was subjected to east–west compression during the Early Yanshanian, resulting in a sinistral strike slip and the derivation of the maximum principal compressive stress in the NEE–SWW direction. The fold axis of the Dahebian syncline is

consistent with the major axis of the strain ellipse (Figure 7a). Therefore, the Dahebian syncline initially took shape under the effect of the first-stage stress field during the Late Jurassic–Early Cretaceous stage (Early Yanshanian), and some thrust faults nearly parallel to the fold axis were formed in association.

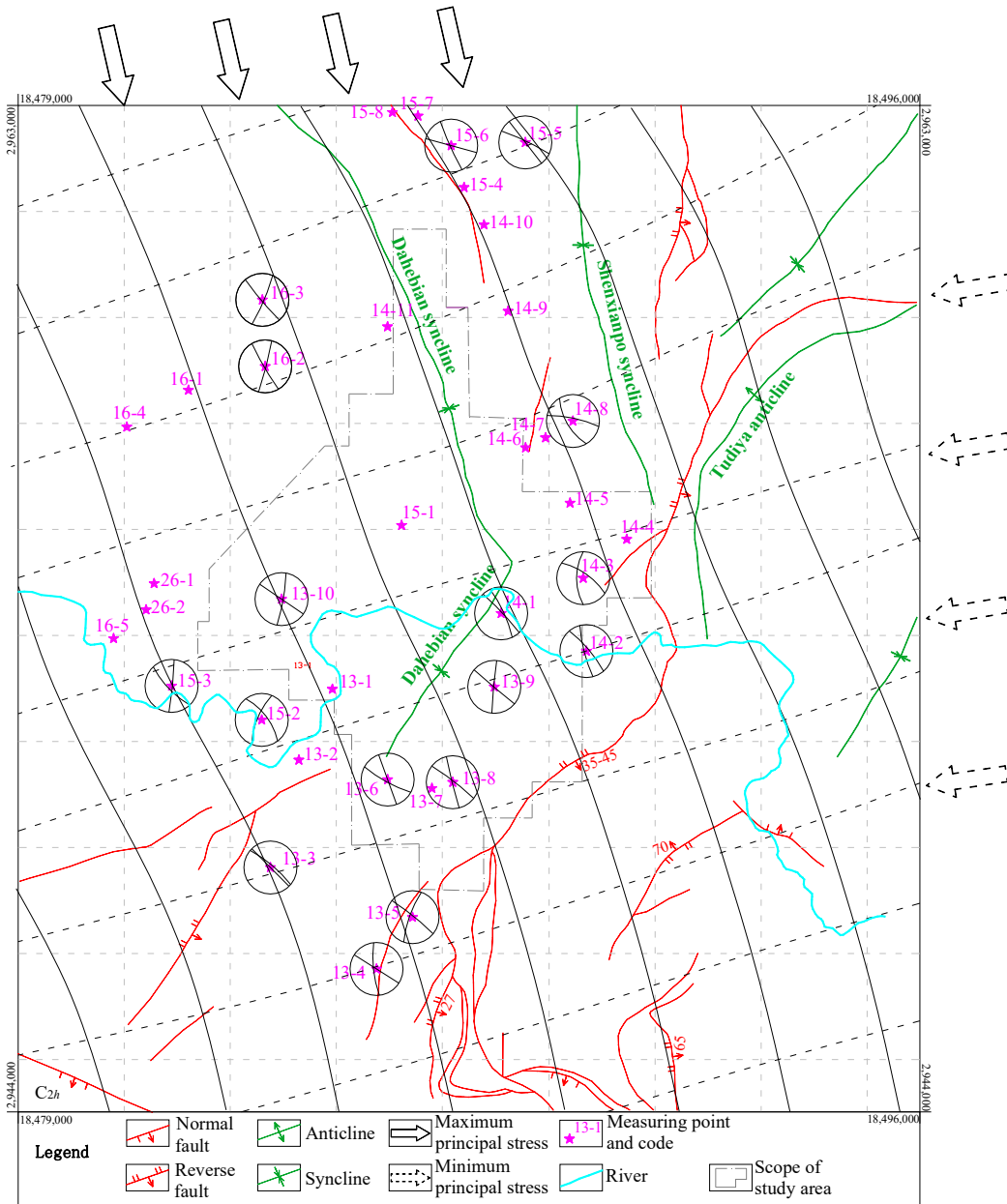
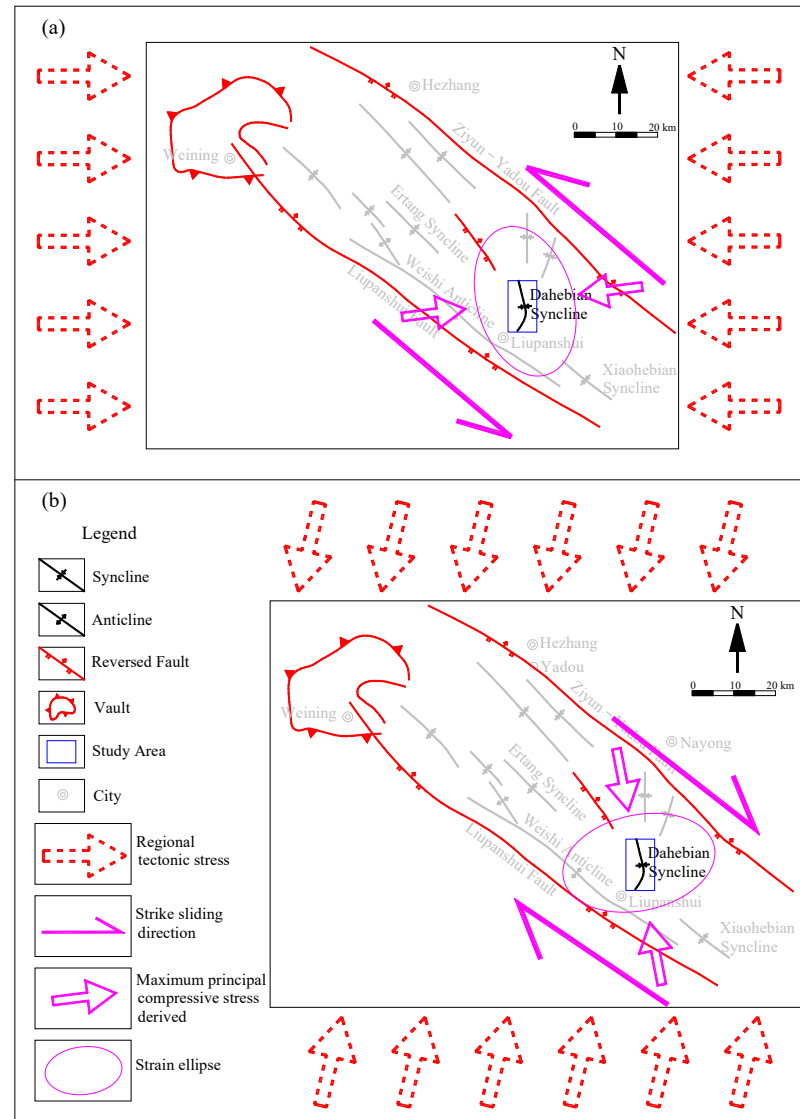


Figure 6. Trace line of the stress field in the second tectonic stage.

During the Late Cretaceous, the orientation of the main compressive stress in the west of the Chinese mainland was NE15° [35], so the WZL fault zone was a dextral strike slip, and the NNW main compressive stress was derived. The stress field in the second stage of the study area was also formed as a result (Figure 7b). Affected by the  $\sigma_1$  in the NNW–SSE direction in the second stage, the fold axis in the south of the study area was deflected in the NE–SW direction, and the strikes of the faults generated in the first stage were also similarly deflected with strike-slip characteristics. During the second stage of tectonic deformation, some new NE–SW strike-slip reverse faults or NW–SE strike-slip normal faults were also formed.

Why is the time constraint of the second-stage stress field believed to be the Late Cretaceous stage and no later? Because in the Cenozoic, the Chinese mainland entered the Himalayan orogenic stage. At that time, the main event in western China was the close of the Yarlung Zangbo Suture Zone. Northeast India edged northward under the Tibet–Yunnan foreland basin. After that time, the uplift in the Qinghai–Tibet Plateau was the main event [36]. Therefore, the study area no longer had the conditions to form NNW-oriented principal compressive stress.



**Figure 7.** Sketch map of tectonic dynamic mechanisms in the study area. (a) The formation mechanism of the tectonic stress field in the Late Jurassic–Early Cretaceous (first stage). (b) The formation mechanism of the tectonic stress field in the Late Cretaceous (second stage).

#### 4. Modern Geostress Field Simulations

##### 4.1. Background of Regional Tectonic Stress Field

The force source of the stress area in eastern China mainly comes from the joint action of the Pacific plate subducting the Eurasian continent in the west and the Philippine plate subducting the Eurasian continent in the northwest. The force source of the tectonic stress area in western China comes mainly from the impact of the Indian plate colliding with Eurasia in the north. At the northern and eastern edges of the Qinghai–Tibet Plateau, the direction of the maximum principal compressive stress of the modern tectonic stress field changes considerably from NNE–SSW to SSE–NNW [37]. The study area is located

in southwest China, close to the front of the Qinghai–Tibet Plateau and the Indian plate. Thus, it is mainly affected by the stress field on the northern and eastern edges of the Qinghai–Tibet Plateau.

According to research on the modern geostress of the coalfield in western Guizhou based on drilling test data collected in the development of the CBM, the direction of the maximum horizontal principal stress in this area shows an obvious NW–SE trend [38]. The magnitude of the principal stress varies with the depth. Generally, there are three stress states. The stress state in shallow areas is  $\sigma_{H_{\max}} > \sigma_{H_{\min}} > \sigma_V$  or  $\sigma_{H_{\max}} > \sigma_V > \sigma_{H_{\min}}$ , and it converts to  $\sigma_V > \sigma_{H_{\max}} > \sigma_{H_{\min}}$  with the depth. It shows a pattern of  $\sigma_{H_{\max}} > \sigma_V > \sigma_{H_{\min}}$  when the stratum depth exceeds 1000 m [39–42].

According to the hydraulic fracturing data of the Liupanshui and Zhina coalfields, the relationship between the maximum horizontal principal stress ( $\sigma_{H_{\max}}$ ) and depth ( $h$ ) is as follows [39]:

$$\sigma_{H_{\max}} = 0.0246h + 2.2598, \quad (1)$$

According to the original rock stress measurement results of Bide coal mine, the relationship between the maximum horizontal principal stress ( $\sigma_{H_{\max}}$ ) and depth ( $h$ ) is as follows [43]:

$$\sigma_{H_{\max}} = 0.0319h + 1.2577, \quad (2)$$

The study area is located in the interior of the Liupanshui coalfield; the Zhina coalfield is the adjacent coalfield to the east of the study area, and the Bide coal mine is located within the Zhina coalfield, with a straight-line distance of only 30 km from the study area. Therefore, the two above fitting equations have high reference values. The average value of the coefficients of the two equations is taken to establish the relationship between the maximum horizontal principal stress and the depth as the boundary condition of the simulated stress field. The equation is as follows:

$$\sigma_{H_{\max}} = 0.0283h + 1.7588, \quad (3)$$

where  $\sigma_{H_{\max}}$  is the maximum horizontal principal stress (MPa), and  $h$  is the depth (m).

#### 4.2. Geological Modeling and Finite Element Simulation of Ground Stress

According to the orientation characteristics of the regional modern stress field, the orientation of the maximum horizontal principal stress in the study area is approximately  $120^\circ$  [37]. Within the scope of the study area, seven geological profiles are identified at equal intervals from north to south. The orientation of the geological profile is parallel to the orientation of the maximum horizontal principal stress in the study area (Figure 8). Based on the above work, seven 2D geometric geological models of the study area were established (Figure 9a).

According to the physical and mechanical properties of rocks, strata with similar mechanical properties were combined into a fixed rock combination, and 13 rock combination layers were divided, including 5 rock formation types: hard, medium hard, medium soft, soft, and extremely soft (Table 1). The calculation parameters of each rock formation were determined according to the lithology and the empirical values of rock mechanical parameters (Table 4).

A finite element simulation of modern geostress in the study area was carried out according to the following steps:

1. Mesh generation: Considering the characteristics of stratum thickness and structural form, the unit division of the thinner rock stratum (or coal seam) was densified, especially the target stratum (coal seam No. 11,  $P_3l$ );
2. Boundary constraints: A vertical constraint was adopted for the bottom boundary ( $U_Y = 0$ ), and a horizontal free constraint was adopted for the lateral boundary (i.e., a roller bearing restraint);

3. Model loading: Horizontal pressure stress loading with a triangular distribution was applied to the models according to Equation (3). The gravitational acceleration was set to  $g = 10 \text{ m/s}^2$  in a vertical direction;
4. Operation and results: The stress and strain values on each node were calculated. As stress includes  $\sigma_1$  and  $\sigma_3$  and equivalent stress, the equivalent stress (i.e., von Mises stress) was used to represent the geostress state (Figure 9b).

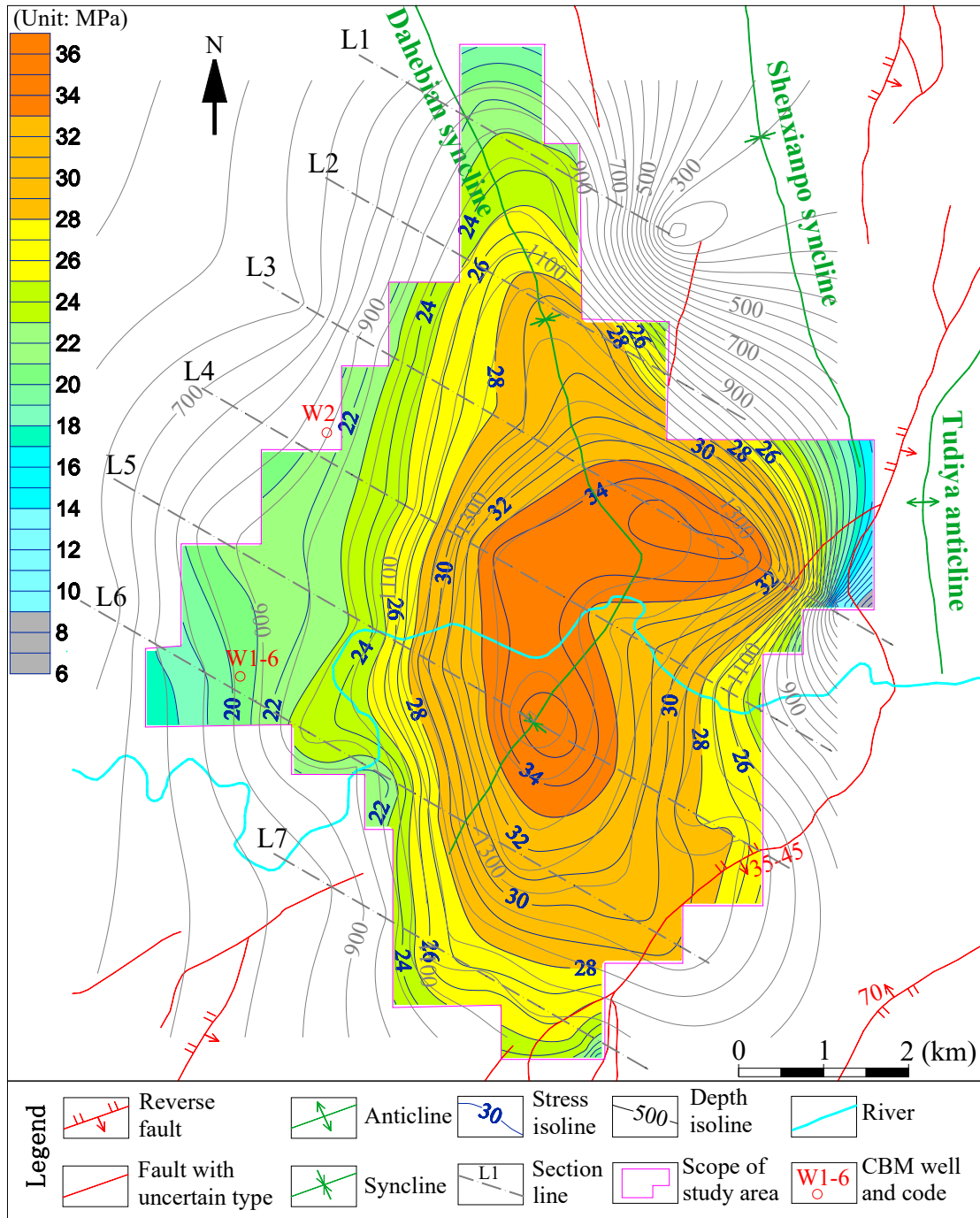
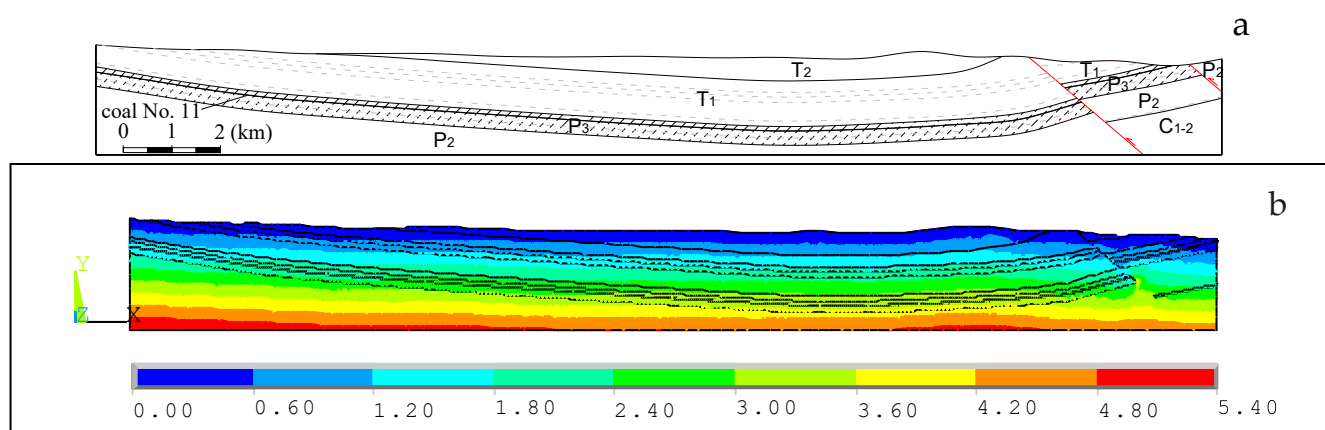


Figure 8. Equivalent stress contour map of coal seam No. 11.



**Figure 9.** Modeling and simulation results of profile L3. (a) The establishment of a 2D geological profile model. (b) An equivalent stress cloud map of a geological profile (units:  $\times 10^8$  Pa).

**Table 4.** Classification of rock assemblage types and simulation calculation parameters in the study area.

Rock Assemblage	Classification	Mechanical Index
Limestone or Emeishan basalt with a single lithology.	Hard	$E = 40 \times 10^9$ , $\mu = 0.28$ , $\rho = 2720$
Mainly sandstone mixed with thin mudstone and sandy mudstone or dolomite and limestone intercalated with argillaceous limestone.	Medium hard	$E = 25 \times 10^9$ , $\mu = 0.33$ , $\rho = 2650$
Siltstone, silty mudstone, and mudstone intercalated with thin to medium-thick layered limestone and argillaceous limestone.	Medium soft	$E = 15 \times 10^9$ , $\mu = 0.36$ , $\rho = 2640$
Coal-bearing strata, including sandy mudstone, mudstone, marlstone, or thin limestone, and siltstone intercalated with thin coal seams.	Soft	$E = 10 \times 10^9$ , $\mu = 0.38$ , $\rho = 2620$
Coal seams and a carbonaceous shale roof.	Extremely soft	$E = 5 \times 10^9$ , $\mu = 0.40$ , $\rho = 1420$

Notes:  $E$  is the modulus of elasticity (Pa);  $\mu$  is Poisson's ratio (dimensionless);  $\rho$  is the density ( $\text{kg}/\text{m}^3$ ).

#### 4.3. Distribution of Geostress of the Target Coal Seam

The stratigraphic profile was divided into many nodes through mesh generation. After being calculated, the nodes were assigned stress and strain values. A contour map of the stress distribution on coal seam floor No. 11 was obtained after collecting node data in the profile line of the coal seam floor from profiles L1–L7 (Figure 8) by kriging interpolation among various profile lines.

According to the statistical data, the maximum equivalent stress of the floor of coal seam No. 11 in the study area is 35.7 MPa, and the minimum is 4.07 MPa. The overall trend of the modern geostress value in the area is similar to the shape of the syncline, which shows that the stress in the center of the syncline is high and decreases outwardly. Affected by fold axis deflection and fault, the high-stress area deflects eastward at the syncline core, showing a “ $\Gamma$ ” form. To the east of the block, the dip angle of the strata is large, and fault influence is observed. The stress gradient is obviously increased, and the stress concentration effect is also displayed near the fault. The dip angle in the west of the block is small, and no fault influence is observed. Thus, the stress gradient is relatively small and stable.

At approximately 1000 m buried depth of coal seam floor No. 11, the equivalent stress is approximately 23 MPa (west of the block) to 26 MPa (east of the block). The equivalent stress continues to increase toward the center of the block and tends to decrease toward its periphery. The vertical stress of coal seam floor No. 11 in the block is greater than the horizontal stress (i.e.,  $\sigma_v > \sigma_{Hmax}$ ). Thus, the  $\sigma_1$  of the coal seam floor in the area is vertical stress.

## 5. Implications for CBM Exploitation

### 5.1. Joint Prediction of Coal Seam

Joint density in sedimentary rocks is highly dependent on many factors, such as tectonic stress, fluid pressure, interbedded layers, and bed thickness [44]. López-Gamundí and Rossello [11] found that there is a good linear correlation between fracture spacing and bed thickness in a coal-bearing strata dominated by sandstone and shale. Ref. [45] studied the relationship between the joint density of sandstone layers and that of the coal seam under the same tectonic background and same thickness, positing that they conform to a power function relationship with a power of less than 1 (Figure 10). Thus, the relationship was obtained between the joint density of the coal seam and that of the sandstone layers in the coal-bearing strata under the same thickness.

$$y_c = 7.173x^{0.168}y_s, \quad (4)$$

where  $y_c$  is the joint density of the coal seam (joints/m), and  $y_s$  is the joint density of sandstone layers with the same thickness as the coal seam (joints/m), which can be obtained according to Equation (5).

$$y_s = 29.591x^{-0.437}, \quad (5)$$

where  $x$  is the thickness of the coal seam or sandstone layer (cm).

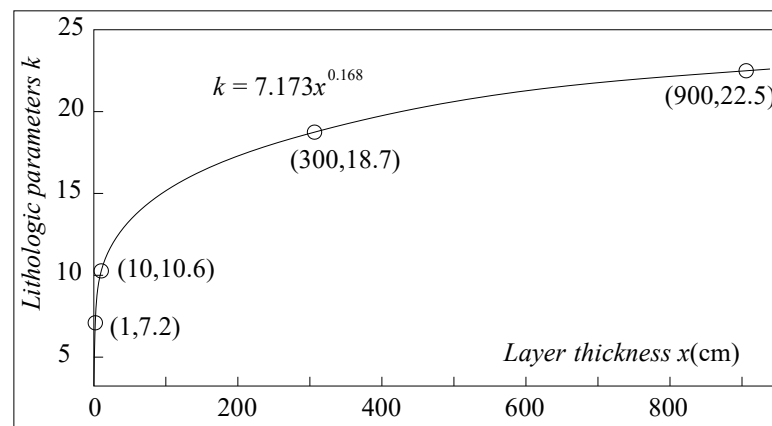


**Figure 10.** Functional relationship between the ratio of the joint density of the coal seam and that of sandstone [45].

Due to the limited number of coal mines in the study area and the lack of permission from coal mine management, it was not possible to conduct large-scale surveys of joints in coal seams underground in the study area. Therefore, the coal seam joint density of some observation points in the study area was predicted according to the contour map of coal thickness using Equation (4). Therefore, the joint density contour map of coal seam No. 11 was drawn (Figure 11a). Given the characteristics of stratigraphic lithology in the study area, the hinterland of the block is a large area of limestone of the Yongningzhen Formation ( $T_{1yn}$ ) and the Guanling Formation ( $T_{2g}$ ), lacking sandstone outcrops. To avoid an uneven distribution of data points, joint data of three limestone outcrops (13-9, 13-10, and 15-1) were selected for interpolation calculation, with other outcrops including sandstone or argillaceous sandstone. According to the contour map that was drawn of the coal seam

joint density, the contour shape was reasonable and showed no distortion because of the data of the three limestone outcrops in the hinterland of the block.

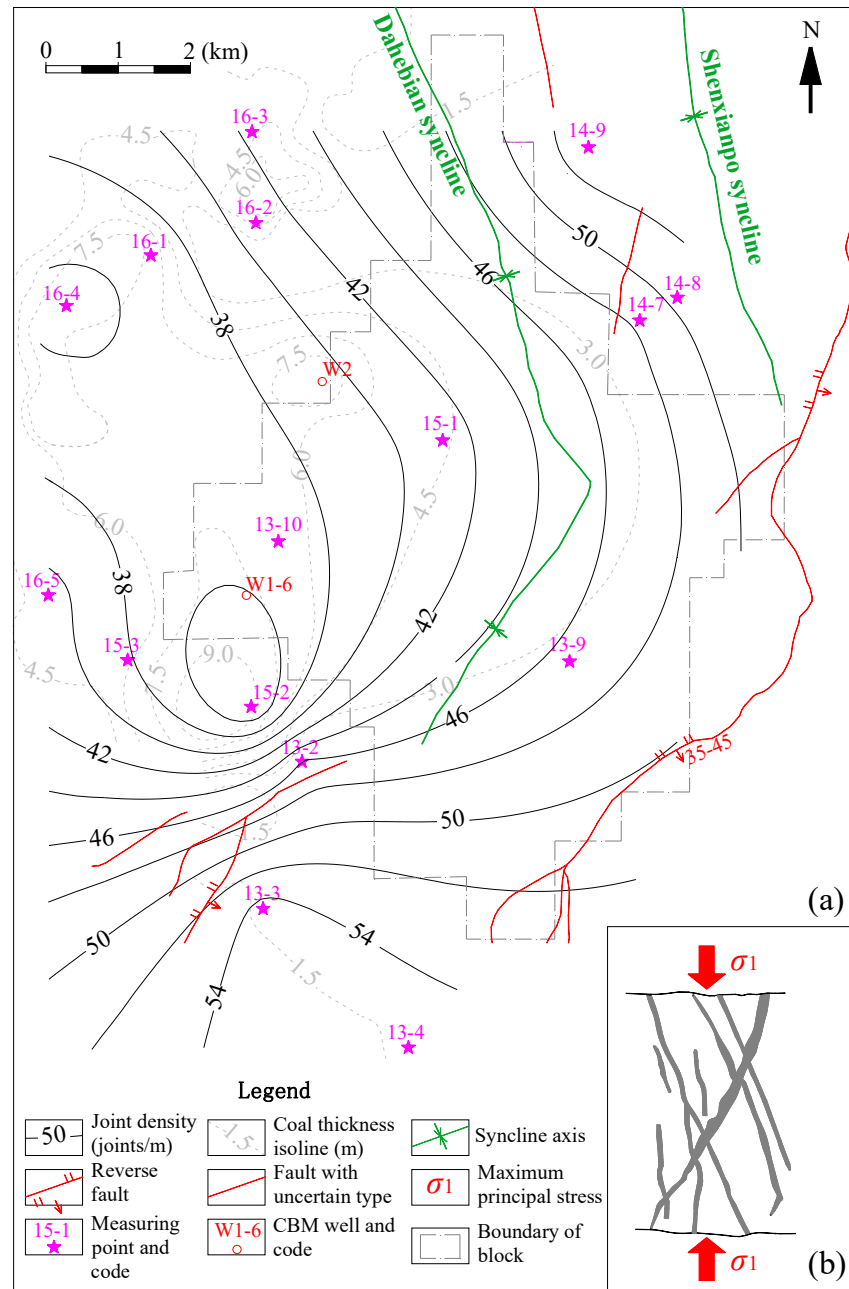


**Figure 11.** Prediction map of occurrence of coal seam joints. (a) Contour map of predicted joint density of the floor of coal seam No. 11. (b) The coal seam joints are sheared first and extended later and are in an open state after progressive deformation.

### 5.2. Discussion of the State of Joints and CBM Exploitation

According to the statistical results with respect to the occurrence of dominant joints in this area, the dominant strikes of rock joints are approximately NW–NNW (300°–360°) and NE (30°–60°) (Figure 3a), and the dip angles of the joints are mostly greater than 60° (Figure 3b). The dominant strikes of coal microfractures are NW (285°–304°) and NE (43°–53°) (Figure 4). First, in the early stage of the Yanshanian (the first stage, i.e., the Late Jurassic–Early Cretaceous) and the late stage (the second stage, i.e., the Late Cretaceous), the coal seams and overlying strata in the study area underwent the same tectonic evolutionary

process and tectonic stress field action. The strike direction of coal microfractures is also very similar to the dominant strikes of the rock joints. Therefore, the coal seam joints and rock strata joints in the study can be considered to have similar occurrences.

According to the numerical simulation results of the modern geostress field, the principal stresses of coal seam No. 11 in the study area show a pattern of  $\sigma_v > \sigma_{Hmax} > \sigma_{Hmin}$ . Based on structural deformation, it is inferred that the dip angle of the coal seam joints is close to the dip angle value of rock seam joints. In other words, the coal seam joints in the study area are speculated to be mostly greater than  $60^\circ$ . Therefore, when  $\sigma_1$  is vertical stress, the deformation of coal seam joints is shear first, then tension, transitioning to an open state due to progressive deformation (Figure 11b). This can help to improve the permeability of the coal reservoir.

According to the prediction results, the joint density of coal seam No. 11 in the block is 36–50 joints/m. The shape of its contour line is jointly influenced by the fold hinge of the Dahebian syncline and surrounding faults. This shows that the contour lines of joint density are roughly similar in shape to the bended syncline axis within the block. Secondly, the density gradient of joints near the faults significantly increases (Figure 11a).

The Dahebian CBM block was assessed as a medium-sized coalbed gas field with medium resource abundance and medium-to-deep burial depth. Through the above analysis of the joints state in the study area, during the development of CBM, the development characteristics of the dominant joints in the study area and the characteristics of the modern geostress field of the coal reservoir should be considered for reservoir fracturing and fissure making. Given that the microfractures in the coal seam in the study area have obvious NW and NE strikes, a better choice would be to use these two orientations alternately as the  $\sigma_1$  orientation of hydraulic fracturing to facilitate the opening of microfractures in the coal seam. In areas with a low joint density of the coal seam, the use of a fracture proppant can be considered.

There are coal mines located around this block, especially in the west and north. Gas drainage is expected to be carried out at the same time as coal mining. Thus, the content of CBM in the area around this block is decreasing. Moreover, the cloud map of equivalent stress shows that the middle part of this block is a high-stress area, and the equivalent stress gradually decreases toward the periphery. The CBM tends to diffuse from high concentrations to low concentrations and migrates from high-stress areas to low-stress areas. Therefore, CBM seepage in the study area should be diffuse and migrate from the basin's center to the periphery.

The above analysis was only conducted from the perspective of the two factors of coal seam fracture and the stress field in the study area. However, the development of CBM is a complex process, and its influencing factors are diverse. In future works, a comprehensive analysis should be carried out on the basis of the above analysis and in combination with consideration of other factors.

### 5.3. Summary and Prospects

- ✧ Innovation point: (1) In this study, we reconstructed the paleotectonic stress field in the study area through the investigation of sedimentary rock joints and clarified the structural evolution of the study area and the genesis mechanism of coal seam joints. The distribution characteristics of geostress in coal reservoirs were revealed through numerical simulation, laying the foundation for the mechanical analysis of coal seam joints. (2) Drawing on the empirical relationship between sedimentary rock joints and coal seam joints previously studied by other researchers, the density of coal seam joints in the study area was predicted. Based on the geostress characteristics of coal reservoirs, the permeability of coal reservoirs and the diffusion trend of CBM were discussed. Combined with the characteristics of the development of joints in the study area, suggestions for hydraulic fracturing technology were proposed.
- ✧ Application: The exploitation of coalbed methane in the study area is still in the initial stage, and there are few relevant production data. Gas production data from two

wells (W2 and W1-6) have been collected to date. CBM production was compared by combining the geostress conditions of two wells (Figure 8) and the density of coal seam joints (Figure 11). To ensure comparability between the two, a comparison was made based on the stable gas production of the two wells in their first year of operation (Table 5). The geostress conditions of the two well locations are very close, and the gas production of the coal seam with a high density of joints (W2 well) is higher than that of the coal seam with low joint density (W1-6 well). Although the amount of available data is currently limited, they at least reflect the contribution of coal seam joint density.

- ✧ Shortcomings: The investigation of coal seam joints is currently very difficult for various reasons. In addition to restrictions on personnel entering the well imposed by management, the following must also be taken into account: (1) The depth of coal seam mining is generally shallow ( $\leq 1000$  m). (2) The distribution range of coal mines is generally limited to the periphery of coal basins, and their quantity is very limited. (3) The coal roadways that have been excavated underground are protected by the use of anchor rods and steel wire mesh, which hinders the measurement of joints. (4) The production cycle of coal mines is very long (at least several decades), and it is unrealistic to conduct investigations of joints on a large number of freshly exposed coal walls in terms of time.
- ✧ Research prospects: It is precisely due to the limitations of the underground investigation of coal seam joints that the study's significance of establishing a correlation between surface rock seam joints and underground coal seam joints is reflected. An outstanding question is how to conduct more in-depth research on coal seam joints (or natural fractures) in the future. We believe the following: (1) Joints themselves are a structural phenomenon, and it is necessary to also strengthen the study of the structural stress field and structural deformation. (2) Numerical simulation methods have considerable advantages; as compared to a limited number of sampling analyses, numerical simulation can demonstrate a wider range of stress and strain states.

**Table 5.** Comparison of gas production and reservoir condition data from two wells.

Well Number	Gas Production in the First Year ( $\text{m}^3/\text{day}$ )	Geostress (MPa)	Coal Seam Joint Density (Joints/m)
W2	2000	21.2	39.8
W1-6	1200	20.4	35.9

Note: The main gas-producing layer of the CBM well is coal seam No.11.

## 6. Conclusions

- (1) The structural evolution of the Dahebian syncline can be divided into two stages. Stage 1: In the Late Jurassic–Early Cretaceous (Early Yanshanian), the WZL fault zone experienced sinistral strike slip, and the derived stress field in the study area showed a  $\sigma_1$  in the NEE–SWW direction and a  $\sigma_3$  in the NNW–SSE direction. The  $\sigma_1$  deflects near the E–W direction in the west–south part of the block and towards the NE–SW direction in the east–north part. Stage 2: In the Late Cretaceous period (Late Yanshanian), the WZL fault zone experienced dextral strike slip, and the derived stress field in the study area showed a  $\sigma_1$  in the NNW–SSE direction and a  $\sigma_3$  in the NEE–SWW direction. The trace of principal stress exhibits certain fluctuations. Under the action of tectonic stress in the second stage, the fold axis in the south was deflected in the NE–SW direction, and the strikes of the faults generated in the first stage also underwent a similar deflection, exhibiting strike-slip properties.
- (2) The joints formed by the two stages of tectonic deformation in the study area are superimposed on each other; the dominant orientations of the joints' strikes in the sedimentary rock strata are approximately NW–NNW ( $300^\circ$ – $360^\circ$ ) and NE ( $30^\circ$ – $60^\circ$ ) in the end. The dip angle of joints in the study area is generally large, and the number

of joints with a dip angle greater than  $60^\circ$  accounts for 70.9%. The dominant strikes of microfractures in the coal seam are NW ( $285^\circ$ – $304^\circ$ ) and NE ( $43^\circ$ – $53^\circ$ ), which are very similar to the dominant strikes of rock joints.

- (3) The maximum equivalent stress of the floor of coal seam No. 11 in the study area is 35.7 MPa, and the minimum is 4.07 MPa. The overall trend of the modern geostress value in the area is similar to the shape of the syncline, showing that the stress in the center of the syncline is high and decreases outwardly. Affected by fold axis deflection and fault, the high-stress area deflects eastward at the syncline core, showing a “T” form. The  $\sigma_1$  of the coal seam floor in the area is vertical stress.
- (4) The coal seam joints in the study area are similar to the rock stratum joints in terms of occurrence, including the dominant orientation and large dip angle. Under vertical stress (also  $\sigma_1$ ), the deformations of coal seam joints are in a tension–shear state, which is conducive to improving the permeability of the coal reservoir. The joint density of coal seam No. 11 in the block is predicted to be 36–50 joints/m, and the shape of its contour line is affected by the axial direction of the Dahebian syncline and the surrounding faults. CBM seepage in the study area is speculated to be diffuse and migrate from the center of the basin to the periphery.

**Author Contributions:** The specific contributions of all authors to the preparation of this manuscript are as follows. J.W.: conceptualization, formal analysis, investigation, methodology, and writing—original draft; Y.W.: investigation, resources, supervision, and validation; X.Z.: project administration, funding acquisition, and writing—review and editing. W.X.: data curation, investigation, and visualization; C.C.: data curation, investigation, and visualization. All authors have read and agreed to the published version of the manuscript.

**Funding:** This research was funded by the National Natural Science Foundation of China (Grant No. 42030810) and The APC was also funded by Grant No. 42030810.

**Data Availability Statement:** Data is contained within the article.

**Conflicts of Interest:** Author Youkun Wang was employed by the company Guizhou Coalbed Methane Energy Development Co., Ltd. The remaining authors declare that the research was conducted in the absence of any commercial or financial relationships that could be construed as a potential conflict of interest.

## References

1. Tan, Y.L.; Pan, Z.J.; Feng, X.T.; Zhang, D.X.; Connell, L.D.; Li, S.J. Laboratory characterisation of fracture compressibility for coal and shale gas reservoir rocks: A review. *Int. J. Coal Geol.* **2019**, *204*, 1–17. [\[CrossRef\]](#)
2. Shi, J.X.; Zeng, L.B.; Zhao, X.Y.; Zhang, Y.Z.; Wang, J.P. Characteristics of natural fractures in the upper Paleozoic coal bearing strata in the southern Qinshui Basin, China: Implications for coalbed methane (CBM) development. *Mar. Pet. Geol.* **2020**, *113*, 104152. [\[CrossRef\]](#)
3. Du, Z.G.; Zhang, X.D.; Huang, Q.; Zhang, S.; Wang, C.L. Investigation of coal pore and fracture distributions and their contributions to coal reservoir permeability in the Changzhi block, middle-southern Qinshui Basin, North China. *Arab. J. Geosci.* **2019**, *12*, 505. [\[CrossRef\]](#)
4. Yang, S.Y.; Cai, Y.D.; Wei, R.; Zhou, Y.F. A new fracture permeability model of CBM reservoir with high-dip angle in the southern Junggar Basin, NW China. *Energy Explor. Exploit.* **2019**, *37*, 125–143. [\[CrossRef\]](#)
5. Zhang, L.H.; Lu, G.; Chang, C.; Wu, J.; Zhao, Y.L.; Liu, W.T. Numerical simulation of a coupled gas flow and geomechanics process in fractured coalbed methane reservoirs. *Energy Sci. Eng.* **2019**, *7*, 1095–1105. [\[CrossRef\]](#)
6. Wu, W.; Yang, S.; Aguilera, R.; Chen, Z.X.; Aguilera, R.F. Characterization methods for natural fractures distribution in shale and tight reservoirs. *Int. J. Coal Geol.* **2023**, *273*, 104252. [\[CrossRef\]](#)
7. Whitaker, A.E.; Engelder, T. Characterizing stress fields in the upper crust using joint orientation distributions. *J. Struct. Geol.* **2005**, *27*, 1778–1787. [\[CrossRef\]](#)
8. Zhang, Z.P.; Wang, Q.C. Development characteristics of joints and shear fractures in Kuqa depression and their implications for regional stress field transformation. *Sci. China Ser. D Earth Sci.* **2004**, *34* Suppl. S1, 63–73. (In Chinese)
9. Gong, W.D. Paleo-tectonic stress field and tectonic evolution since the Mesozoic in the eastern mining area of Pingdingshan. *Earth Sci. Res. J.* **2019**, *23*, 347–357. [\[CrossRef\]](#)
10. Ju, W.; Hou, G.T.; Li, L.; Xiao, F.F. End Late Paleozoic tectonic stress field in the southern edge of Junggar Basin. *Geosci. Front.* **2012**, *3*, 707–715. [\[CrossRef\]](#)

11. López-Gamundí, O.R.; Rossello, E.A. The Permian Tunas Formation (Claromecó Basin, Argentina): Potential naturally fractured reservoir and/or coal bed methane (CBM) play? *Mar. Pet. Geol.* **2021**, *128*, 104998. [[CrossRef](#)]
12. Su, N.; Zou, L.J.; Shen, X.H.; Wu, W.Y.; Zhang, G.F.; Kong, F.L.; Zhang, Z.; Dong, Y.P.; Xiao, A.C. Identification of fracture development period and stress field analysis based on fracture fabrics in tectonic superposition areas. *Arab. J. Geosci.* **2014**, *7*, 3983–3994. [[CrossRef](#)]
13. Chen, L. Tectonic stress reconstruction based on structural features in tectonic superposition areas. *Min. Metall. Explor.* **2020**, *37*, 387–397.
14. Ramsay, J.G.; Huber, M.I. *The Techniques of Modern Structural Geology, Folds and Fractures*; Academic Press: London, UK, 1987; Volume 2, pp. 641–666.
15. Maerten, L.; Maerten, F. Chronologic modeling of faulted and fractured reservoirs using geomechanically based restoration: Technique and industry applications. *AAPG Bull.* **2006**, *90*, 1201–1226. [[CrossRef](#)]
16. Li, J.J.; Qin, Q.R.; Li, H.; Zhou, J.L.; Wang, S.T.; Zhao, S.X.; Qin, Z.J. Numerical simulation of the palaeotectonic stress field and prediction of the natural fracture distribution in shale gas reservoirs: A case study in the Longmaxi Formation of the Luzhou area, southern Sichuan Basin, China. *Geol. J.* **2023**. *early access*. [[CrossRef](#)]
17. Liu, J.S.; Ding, W.L.; Yang, H.M.; Jiu, K.; Wang, Z.; Li, A. Quantitative prediction of fractures using the finite element method: A case study of the lower Silurian Longmaxi formation in northern Guizhou, South China. *J. Asian Earth Sci.* **2018**, *154*, 397–418. [[CrossRef](#)]
18. Wang, J.L.; Li, M.; Xu, S.C.; Qu, Z.H.; Jiang, B. Simulation of ground stress field and advanced prediction of gas outburst risks in the non-mining area of Xinjing Mine, China. *Energies* **2018**, *11*, 1285. [[CrossRef](#)]
19. Xu, M.; Yang, J.W.; Jia, S.P.; Chen, Z.L. Finite element back analysis of geostress field in geological body of oil and gas trap. *Acta Geodyn. Geomater.* **2022**, *19*, 143–154. [[CrossRef](#)]
20. Wang, L.L.; Jiang, B.; Wang, J.L.; Wang, J.Y.; Qu, Z.H. Effects of in-situ stress and joint on permeability of the coal bed in Linfen block, southeastern Ordos basin, China. *Russ. Geol. Geophys.* **2018**, *59*, 299–312. [[CrossRef](#)]
21. Liu, H.H.; Sang, S.X.; Xue, J.H.; Wang, G.X.; Xu, H.J.; Ren, B.; Liu, C.J.; Liu, S.Q. Characteristics of an in situ stress field and its control on coal fractures and coal permeability in the Gucheng block, southern Qinshui Basin, China. *J. Nat. Gas Sci. Eng.* **2016**, *36*, 1130–1139. [[CrossRef](#)]
22. Fu, X.L.; Dai, J.S.; Feng, J.W. Prediction of tectonic fractures in coal reservoirs using geomechanical method. *Geosci. J.* **2018**, *22*, 589–608. [[CrossRef](#)]
23. Ju, W.; Wang, K.; Hou, G.T.; Sun, W.F.; Yu, X. Prediction of natural fractures in the Lower Jurassic Ahe Formation of the Dibeil Gasfield, Kuqa Depression, Tarim Basin, NW China. *Geosci. J.* **2018**, *22*, 241–252. [[CrossRef](#)]
24. Huang, S.P.; Liu, D.M.; Yao, Y.B.; Gan, Q.; Cai, Y.D.; Xu, L.L. Natural fractures initiation and fracture type prediction in coal reservoir under different insitu stresses during hydraulic fracturing. *J. Nat. Gas Sci. Eng.* **2017**, *43*, 69–80. [[CrossRef](#)]
25. Li, Y.W.; Jia, D.; Li, W.; Zhang, K.P. Model of T-type fracture in coal fracturing and analysis of influence factors of fracture morphology. *Energies* **2018**, *11*, 1196. [[CrossRef](#)]
26. Gao, D.; Qin, Y.; Yi, T.S. CBM geology and exploring-developing stratagem in Guizhou Province, China. In Proceedings of the International Conference on Mining Science & Technology (ICMST2009), Xuzhou, China, 18–20 October 2009; Volume 1, pp. 882–887.
27. Chen, B.Y.; Stuart, F.M.; Xu, S.; Györe, D.; Liu, C.Q. The effect of Cenozoic basin inversion on coal-bed methane in Liupanshui Coalfield, Southern China. *Int. J. Coal Geol.* **2022**, *250*, 103910. [[CrossRef](#)]
28. Yue, G.Y. A new discussion on the structural pattern of Liupanshui area. *Geol. Guizhou* **1991**, *8*, 289–300. (In Chinese with English Abstract)
29. Yue, G.Y.; Zhang, S.J.; Yang, W.N. Structural deformation patterns and tectonic stress field in west-central Guizhou. *Sci. Geol. Sin.* **1994**, *29*, 10–18, (In Chinese with English Abstract).
30. Zhang, R.Q.; Zhou, Y.; Wang, X.W.; Li, S.J.; Li, S. Structural features and tectonic evolution of the Weiziluo fault zone in southwestern Guizhou province. *J. Geomech.* **2009**, *15*, 178–189, (In Chinese with English Abstract).
31. Zhu, H.Z.; Liu, P.; Chen, P.; Kang, J.N. Analysis of coalbed methane occurrence in Shuicheng Coalfield, southwestern China. *J. Nat. Gas Sci. Eng.* **2017**, *47*, 140–153. [[CrossRef](#)]
32. Dou, X.Z. Tectonic Evolution and Its Control on Coalbed Methane Reservoiring in Western Guizhou. Ph.D. Thesis, China University of Mining and Technology, Xuzhou, China, 2012; pp. 22–27, (In Chinese with English Abstract).
33. Wang, Y.; Du, W.; Wang, Y.Y.; Lin, R.Q.; Zhang, D.Q.; Zhao, F.P.; Sun, Z.; Chen, Y.; Wang, Y. Meso-cenozoic tectonic evolution of the Ziyun-Luodian fault in SW China. *Front. Earth Sci.* **2022**, *10*, 970944. [[CrossRef](#)]
34. Dong, S.W.; Zhang, Y.Q.; Long, C.X.; Yang, Z.Y.; Ji, Q.; Wang, T.; Hu, J.M.; Chen, X.H. Jurassic Tectonic Revolution in China and New Interpretation of the Yanshan Movement. *Acta Geol.* **2007**, *81*, 1449–1461, (In Chinese with English Abstract).
35. Wan, T.F.; Zhu, H. The Tectonic Stress Field of the Cretaceous—Early Eocene in China. *Acta Geol.* **1989**, *63*, 14–25. (In Chinese with English Abstract)
36. Wang, H.Z.; Mo, X.X. An outline of the tectonic evolution of China. *Episodes* **1995**, *18*, 6–16. [[CrossRef](#)] [[PubMed](#)]
37. Xie, F.R.; Cui, X.F.; Zhao, J.T.; Chen, Q.C.; Li, H. Regional division of the recent tectonic stress field in China and adjacent areas. *Chin. J. Geophys.* **2004**, *47*, 654–662. (In Chinese with English Abstract)

38. Ju, W.; Yang, Z.B.; Qin, Y.; Yi, T.S.; Zhang, Z.G. Characteristics of in-situ stress state and prediction of the permeability in the Upper Permian coalbed methane reservoir, western Guizhou region, SW China. *J. Pet. Sci. Eng.* **2018**, *165*, 199–211. [[CrossRef](#)]
39. Xu, H.J.; Sang, S.X.; Yang, J.F.; Jin, J.; Hu, Y.B.; Liu, H.H.; Ren, P.; Gao, W. In-situ stress measurements by hydraulic fracturing and its implication on coalbed methane development in Western Guizhou, SW China. *J. Unconv. Oil Gas Resour.* **2016**, *15*, 1–10. [[CrossRef](#)]
40. Chen, S.D.; Tang, D.Z.; Tao, S.; Xu, H.; Zhao, J.L.; Fu, H.J.; Ren, P.F. In-situ stress, stress-dependent permeability, pore pressure and gas-bearing system in multiple coal seams in the Panguan area, western Guizhou, China. *J. Nat. Gas Sci. Eng.* **2018**, *49*, 110–122. [[CrossRef](#)]
41. Fang, X.; Wu, C.; Jiang, X.; Liu, N.; Zhou, D.; Ju, Y. Characteristics of in situ stress and its influence on coal seam permeability in the Liupanshui Coalfield, Western Guizhou. *Energy Sci. Eng.* **2021**, *9*, 1773–1786. [[CrossRef](#)]
42. Chen, S.D.; Tang, D.Z.; Tao, S.; Liu, P.C.; Mathews, J.P. Implications of the in situ stress distribution for coalbed methane zonation and hydraulic fracturing in multiple seams, western Guizhou, China. *J. Pet. Sci. Eng.* **2021**, *204*, 108755. [[CrossRef](#)]
43. Jiang, Y.D.; Zhou, W.X.; Mei, S.X.; Hu, J.; Zhang, Y.G.; Chen, W.; Xiong, L. Test and distribution rule of strata stress field in Bide coal mine. *Min. Saf. Environ. Prot.* **2011**, *1*, 1–3. (In Chinese with English Abstract)
44. Eyssautier-Chuine, S.; Odonne, F.; Massonnat, G. Control of bioclast abundance on natural joint density in carbonate rocks: Data from Oman, Provence and Languedoc (France). *Terra Nova* **2002**, *14*, 198–204. [[CrossRef](#)]
45. Wang, L.L. Evaluation of Joint Development Heterogeneity of Coal Reservoir Based on Structural Dynamics and Its Application: An example from Linfen, the Eastern Margin of the Ordos Basin. Ph.D. Thesis, China University of Mining and Technology, Xuzhou, China, 2014; pp. 89–98. (In Chinese with English Abstract)

**Disclaimer/Publisher’s Note:** The statements, opinions and data contained in all publications are solely those of the individual author(s) and contributor(s) and not of MDPI and/or the editor(s). MDPI and/or the editor(s) disclaim responsibility for any injury to people or property resulting from any ideas, methods, instructions or products referred to in the content.